IEEE Access
Multidisciplinary | Rapid Review | Open Access Journal

Received May 8, 2020, accepted May 31, 2020, date of publication June 5, 2020, date of current version June 18, 2020.

Digital Object Identifier 10.1109/ACCESS.2020.3000329

A Novel Shared Guidance Scheme for Intelligent Haptic Interaction Based Swarm Control of Magnetic Nanoparticles in Blood Vessels

MYUNGJIN PARK[1], TUAN-ANH LE[1], AMRE EIZAD[2], AND JUNGWON YOON[1], (Member, IEEE)
[1]School of Integrated Technology, Gwangju Institute of Science and Technology, Gwangju 61005, South Korea
[2]School of Mechanical and Aerospace Engineering, Gyeongsang National University, Jinju 52828, South Korea

Corresponding author: Jungwon Yoon (jyoon@gist.ac.kr)

This work was supported in part by the National Research Foundation (NRF) of Korea under Grant 2019M3C1B8090798, and in part by the Korea Evaluation Institute of Industrial Technology (KEIT) under Grant 20003822.

ABSTRACT Swarm magnetic control is a promising technology for use in nanorobotics. However, automated control schemes for small and large populations of nanoparticles are not effective due to the complexity of real blood vessels, the lack of technologies for motion control feedback of individual particles, and the inaccuracy of the mathematical models. It is quite difficult to control unexpected magnetic particle movements in a real vessel. Specifically, when magnets are used to guide the particles, the sticking of particles to vessel walls causes the dispersion of particles, which is the main reason for low steering efficiency that may cause the occurrence of side effects in non-targeted areas. In addition, when the aggregation of particles occurs inside the vessels, it can cause clogging of the vessel and the randomness of aggregation makes it difficult for the user to control the particles precisely. In the presented work, we suggest a novel intuitive shared guidance scheme for 3D steering of magnetic nanoparticles (MNPs) in a realistic vessel model. We have performed simulation based user studies with different guidance modes (visual feedback (V), shared control (S), shared control and forbidden region mode (S-F), shared control and adaptive forbidden region mode (S-AF)). The results of these studies show that the suggested S-AF mode can significantly (p-value $<$ 0.01) increase the delivery rate of MNPs to the target region while significantly (p-value $<$ 0.01) reducing the sticking rate of MNPs inside the vessel. The proposed intelligent navigation scheme for MNPs can in the future be combined with real-time magnetic particle imaging (MPI) for targeted drug delivery.

INDEX TERMS Magnetic targeted drug delivery, haptic intelligence, swarm control, shared system.

I. INTRODUCTION

Nanoparticles have attracted extensive attention due to their great promise for biomedicine applications such as high precision targeted delivery and nano-manipulation [1]–[4]. Due to the use of magnetic fields that can penetrate deep tissues and even at relatively high intensities can be considered safe for living beings, magnetic targeted delivery (MTD) using nanoparticles is considered advantageous as compared to the various other targeted delivery approaches [4]–[10]. However, due to the small volume and surface area of a single nanoparticle, targeted delivery tasks may require a swarm of particles for enough actuation forces [11]. Furthermore, *in-vivo* tracking of a single particle is not possible due to the insufficient imaging resolution [12]. Therefore, a method for efficient simultaneous locomotion control of a swarm of nanoparticles is required. For this purpose, the scheme of swarm control at a small scale has become an important emerging technology [13], [14]. Unlike the centimeter or millimeter scale robots that are equipped with various sensors and can be actuated individually [15] or in the form of distributed actuator networks [16], nanoscale robots do not have any onboard sensors and actuators for individual motion feedback and control. Thus, due to these complexities, there are only a few studies related to navigation, control and automated monitoring of the collective behavior of

The associate editor coordinating the review of this manuscript and approving it for publication was Chaitanya U. Kshirsagar.

nanoparticle swarms [17], [18]. These studies mostly employ an open-loop motion control strategy for the steering of the nanoparticles [19]. In the published works, magnetic fields were either preset or manually controlled to guide the swarms to the desired position in two-dimensional (2-D) and three-dimensional (3-D) vessel models [20]–[22]. The results of these studies show effective locomotion but the trajectory tracking accuracy is low and careful tuning of magnetic field parameters is required [23]. In contrast, automated motion control of nanoparticle swarms provides autonomy, high efficiency, and accuracy for performing MTD tasks [24]. For conventional automated control methods, clear mathematical models are usually required [22]. However, for a magnetic nanoparticle swarm, the particles are subject to global magnetic and particle-particle magnetic interaction forces, fluidic forces, and induced interaction forces with geometric environments, that make the development of a precise mathematical model very complex.

In contemporary medical service robotics, it is considered beneficial to have a human operator in the control loop, such as in the teleoperation control approach used in the da Vinci surgical robot [25]. Based on this observation, we previously developed a system utilizing a haptic human interface device for the guidance of MNPs for targeted drug delivery in a simulated 2-D vessel environment, which showed improvement in the targeting ratio [26]. Haptic technologies are used mainly for training and for teleoperation control in virtual environments (VE) [26]–[29]. Haptic force feedback can improve the ability to perform certain tasks in environments where visual feedback is limited [30]. One method for introducing physical limitations in a VE is the application of forbidden regions to limit the user's movements. The forbidden region concept was first introduced by Rosenberg [31] to improve human-machine collaboration in the performance of a specific task by limiting the workspace in the VE. Forbidden regions can be applied to surgery or to any other tasks that require human-robot cooperation [32]. Therefore, MTD can also benefit from the application of the forbidden region concept [33].

However, in existing work [33], the forbidden region concept is applied with the limitation that the forces acting on the particles are reduced to only the drag force and the magnetic force, and the aggregation and sticking of particles are not considered. Furthermore, due to the simplified fluid dynamics, the velocity information at the blood vessel bifurcations does not match the real environment, and the simulations are limited to only a 2D multi-channel case. Thus, when considering the realistic variety of forces acting on particles inside a blood vessel, the forbidden regions concept becomes insufficient, which can eventually reduce the targeting efficiency [21], [22]. Moreover, when expanding from a 2-D to a 3-D environment, the visual limitation due to the geometric structure of vessels may also significantly reduce the targeting efficiency.

The abovementioned limitations can be overcome by involving automatic position control in the overall guidance scheme. The benefit of using a shared control approach for the guidance of rigid hand-held tools has been demonstrated in the context of vitreoretinal surgery [34], [35]. The existing studies on shared-control have mostly focused on magnetic catheter control to allow high dexterity and compliance combined with cooperative control of the tool [36]. However, as per our knowledge there are as yet no studies related to shared control of nanoparticle swarms.

In this research, we have proposed a novel intelligent shared swarm guidance scheme of MNPs that combines an automatic positioning control for simplification of MNP guidance in a realistic 3-D blood vessel with an adaptive forbidden region (AF) to aid the operator by adjusting the forbidden region based on the amount of aggregation of MNPs inside the blood vessel. Furthermore, by combining this control scheme with user feedback control, we have developed a real-time 3-D navigation system for control of MNP swarms inside 3-D blood vessels. In the developed system, the automatic position control confines the 3-D movements of the particles to a 2-D plane, thus simplifying their steering. Due to this simplification, the user can easily utilize the haptic interface device to perform MNP swarm guidance while dealing with the sticking of MNPs. The AF are positioned while considering the particle aggregation. The haptic feedback generated according to the AF allows the user to tune their control input according to the overall dispersion of particles that includes unexpected particle movements at different velocities caused by the aggregation of particles. Thus, the system can help increase the targeting ratio of MNPs. Moreover, the proposed real-time MNP navigation simulator can simulate realistic dynamics of MNPs inside blood vessels. This simulator combines a multi-physics commercial simulation tool (COMSOL^{TM}) for simulating the fluid dynamics inside the blood vessel, and a custom developed physics engine to simulate the behavior of MNPs based on the forces acting on them. These modules are interfaced with a haptics engine and a graphical display to allow input from the user, and visual and haptic feedback to the user.

The remaining parts of this article are structured as follows. Section II describes the dynamic modeling of nanoparticles inside the vessel. Section III introduces the system overview including the closed-loop control system. The adaptive forbidden region algorithm is introduced in Section IV. Section V presents the shared-control algorithm. Section VI presents the evaluation of the efficiency and functionality of the algorithms in a realistic 3-D vessel model. Finally, Section VII concludes this article and describes the future work.

II. DYNAMIC MODEL OF MNPs IN A MAGNETIC DRUG DELIVERY SYSTEM

There are many forces acting on particles moving inside the vessels, including hydrodynamic drag, inertia, buoyancy, gravity, adhesion and contact force. This section describes the modeling of these parameters and the associated equations. The forces acting on a particle are defined according to [21].

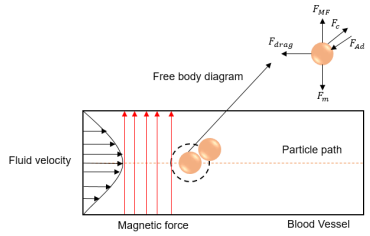

FIGURE 1. Free-body diagram of the forces acting on a particle.

TABLE 1. Parameters used in the simulation.

PARAMETER	Value
MNP initial radius (r_i)	400nm
Blood viscosity	0.004Pa·s
μ_0	$4\pi \times 10^{-7} N/A^2$
M_{sat}	570.7kA/m
Particle density (ρ)	6450 kg/m^3
Maximum diameter (P_l)	5.6μm

Figure 1 provides a pictorial description of these forces and their associated units are given in Table 1. The total force acting on a particle is given as:

$$m_i \frac{\boldsymbol{dv}_i}{\boldsymbol{dt}} = \boldsymbol{F}_{\mathrm{MF}} + \boldsymbol{F}_{\mathrm{drag}} + \boldsymbol{F}_{\mathrm{C}} + \boldsymbol{F}_{\mathrm{Ad}} + \boldsymbol{F}_{\mathrm{m}} \tag{1}$$

where m_{i} and $\boldsymbol{v}_{\mathrm{i}}$ are the mass and velocity of the index i particle, $\boldsymbol{F}_{MF}$ is the magnetic force, $\boldsymbol{F}_{drag}$ is the hydrodynamic drag force, $\boldsymbol{F}_m$ is the gravitational force, $\boldsymbol{F}_C$ is the contact force and $\boldsymbol{F}_{Ad}$ is the adhesion force.

The magnetic force is the only controlled parameter in this system and can be expressed as:

$$\boldsymbol{F}_{MF} = \frac{4}{3}\pi \mu_0 r_{eq}^3 \boldsymbol{M}(\boldsymbol{H}) \cdot \nabla \boldsymbol{H} \tag{2}$$

where μ_0 is the permeability of free space, $\boldsymbol{M}$ is the net magnetic polarization, $\boldsymbol{H}$ is the magnetic intensity, r_{eq} is the equivalent radius of aggregated particle which is explained in section IV, and $\nabla \boldsymbol{H}$ is the gradient of magnetic intensity. If MNPs are magnetically soft and the magnetic field is strong, the net magnetic polarization (M) will be saturated. In this simulation, MNPs are always exposed to a strong magnetic force, so we assume that M has a constant saturated value (M_{sat}). Thus, using a haptic device, we can change the value of the gradient of magnetic intensity to control the nanoparticles inside the vessels.

The drag (hydrodynamic) force acting on a spherical particle, based on Stokes law, is represented as:

$$\mathrm{F}_{\mathrm{drag}} = -6\pi \eta r_{eq}(v_p - v_f) \tag{3}$$

where $\boldsymbol{v}_{\mathrm{p}}$ and $\boldsymbol{v}_{\mathrm{f}}$ are the velocities of the particle and fluid, respectively, r_{eq} is the equivalent radius of aggregated particle and η is the fluid viscosity.

The gravity and buoyancy forces acting on the particle are combined and represented as the net gravitational force:

$$\mathrm{F}_{\mathrm{m}} = \frac{4}{3}\pi r_{eq}^3 \left(\rho_p - \rho_b\right) \boldsymbol{G} \tag{4}$$

where ρ_{p} and ρ_{b} are the densities of the particle and the fluid (blood), respectively, r_{eq} is the equivalent radius of aggregated particle and $\boldsymbol{G}$ is the gravitational force.

Contact forces are generated as a result of particle-particle or particle-vessel collisions. The particle-particle collisions can be expressed using the Hertzian contact model:

$$\boldsymbol{F}_{\mathrm{C}} = k\boldsymbol{\delta}^{\frac{3}{2}} \leftrightarrow d < R_i + R_j \tag{5}$$

where d is the distance between particles i and j, R_i *is* the radius of the i^{th} particle, R_j is the radius of the j^{th} particle, k is the spring constant of the particle, and δ is the deformation of the particle.

Nowadays, the effects of adhesion have become quite reduced due to the improvement in nanoparticle coating techniques [37]. However, the sticking of particles to other surfaces cannot be completely eliminated by coatings. Thus, the adhesion force is given as:

$$\boldsymbol{F}_{\mathrm{Ad}} = \tau \pi R^3 \left(\frac{3\boldsymbol{F}_{\mathrm{C}} R}{4\boldsymbol{E}^*}\right) \tag{6}$$

where τ is the adhesive energy (a constant), R is the equivalent radius of two particles at the moment of attachment (7), $\boldsymbol{F}_{\mathrm{C}}$ is the contact force, and $\boldsymbol{E}^*$ is the equivalent elasticity module (8).

$$R = \frac{R_i R_j}{R_i + R_j} \tag{7}$$

Here, R_{i} and R_{j} are the radii of the i^{th} and j^{th} particles, respectively.

$$\frac{1}{\boldsymbol{E}^*} = \frac{1 - v_i^2}{E_i} + \frac{1 - v_j^2}{E_j} \tag{8}$$

Here, E_i and E_j are the elasticity moduli of the i^{th} and j^{th} particles, respectively, and v_i and v_j are the Poisson's ratios of the i^{th} and j^{th} particles, respectively.

In nature, the contact force generally works to detach the particles while the adhesion force works to attach them. Thus, the opposite nature of the contact and adhesion forces results in two possible outcomes; attachment or detachment.

III. VIRTUAL GUIDANCE SYSTEM FOR MNPs

A. SYSTEM OVERVIEW

Exploiting the advances in virtual reality (VR) technologies, virtual environment (VE) simulations in a manner similar to the physical tele-nano-manipulation system can replicate real in vivo experiments without requiring the implementation of the entire hardware systems. Using this method, we can get an objective analysis of haptic guidance effects during the tele-operated interactions of a user for manipulations of MNPs inside virtual environments. Our proposed system, shown in Figure 2, consists of a virtual environment that provides visual information about the vessel structure and the positions of particles inside it. And a haptic device that is used by the user to guide the particles. The haptic device can also provide haptic feedback to the user according to the particular control methodology being used.

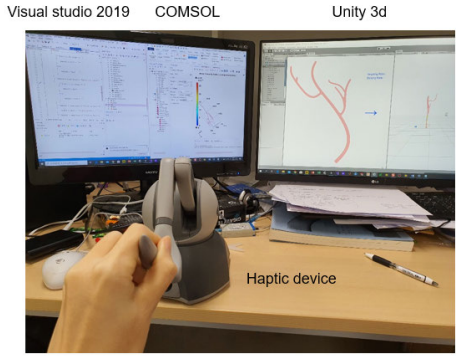

FIGURE 2. Overall tele-nano-manipulation system.

We have implemented a three-dimensional MNP guidance simulator that includes a graphic engine, a haptic engine and a physics engine, as shown in Figure 3. The physics engine generates the particle movements inside the vessel model based on the fluid and particle dynamics and the control input from the user. The haptic engine interfaces the software with the haptic device taking the haptic device position as input and generating haptic feedback force commands as output. The graphic engine generates the visual feedback provided to the operator which contains a depiction of the vessel model showing the positions of all the particles inside it. The graphic engine is developed using the Unity 3D environment while the haptic and physics engines are developed using C# programming in Visual Studio 2019. An overview of the system architecture including data flow and update rates of the engines is presented in Figure 3.

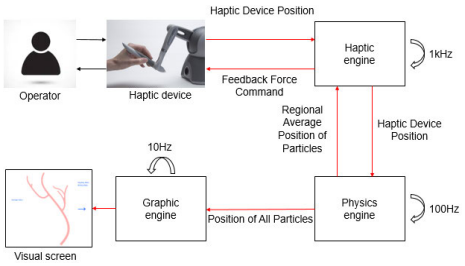

FIGURE 3. Virtual guidance system overview.

The haptic engine operates at 1000 Hz (haptic system frame rate). It reads the haptic device position and relays it to the physics engine. It also generates feedback force commands for the device based on the position of the regional average, which is described later in this article. The physics engine, which operates at a rate of 100Hz due to processing capacity limitations takes the haptic device position as input. It determines the particle positions according to the haptic device position and the fluid dynamics. It also calculates the particle regional average position, which is transmitted to the haptic engine. The positions of all the particles are transmitted to the graphic engine. The graphic engine receives the particle positions data and updates the visual display accordingly at a rate of 10 Hz (set due to processing limitations). This update rate is double of what has previously been reported for *in-vitro* testing of a developed targeted drug delivery system [38].

B. PHYSYICS ENGINE ALGORITHM

Figure 4 shows the flowchart of the proposed simulation system. The mapping and haptic feedback units are shown in Figure 4(a). The mapping unit enables the user to steer the MNPs by changing the magnetic force according to the haptic device position. The haptic rendering unit takes the average position of MNPs as the input and orders the delivery of haptic force to the user when the MNPs make contact with the forbidden region. The magnetic force mapped to the haptic device movements acts as the input for the physics engine. As shown in Figure 4(b), before starting the simulation the user sets the simulation parameters. Based on these parameters, prior to the start of simulation, the fluid velocity profile is generated using COMSOL and exported to Unity 3D (Visual Studio) in the form of a MS Excel spreadsheet. In Unity 3D, when simulation starts, the drag force is calculated based on this fluid velocity profile and the magnetic force is applied according to the haptic device position obtained from the haptic engine. During simulation, when a particle collides with another particle, one of two possible outcomes occurs. Either the particles become attached to form an aggregate

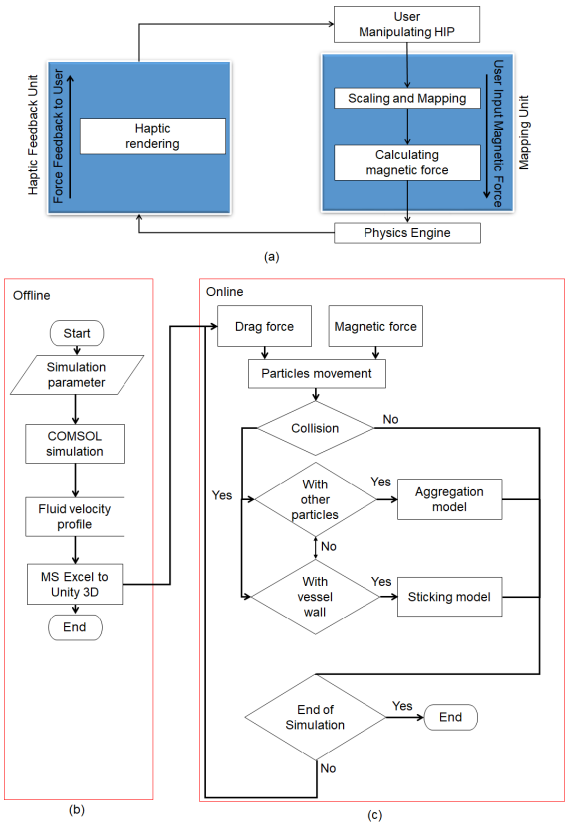

FIGURE 4. Flow chart of the simulation. (a) haptic engine for tele-manipulation of magnetic nanoparticles (MNPs), (b) offline and (c) online parts of the physics engine.

or they remain separate. Aggregation occurs if the adhesion force is greater than the contact force ($F_C < F_{Ad}$), defined in (5) and (6). If the opposite ($F_C > F_{Ad}$) is true, then attachment does not occur. When attachment occurs, the equivalent spherical radius of the aggregate thus formed is different from the original particles, but is not equal to the sum of the original radii [21]. To quantify the change in the equivalent spherical radius due to aggregation, an aggregation model is proposed in this research, which is explained in detail in section IV A. When a particle-vessel collision occurs, the three forces applied are given by equations (2), (5) and (6). We have assumed that the vessel wall is smooth. So, if the adhesion force between particle and the vessel wall is higher than the magnetic force ($\boldsymbol{F}_c + \boldsymbol{F}_{MF} < \boldsymbol{F}_{Ad}$), the particles will stick to the vessel wall. If not ($\boldsymbol{F}_c + \boldsymbol{F}_{MF} > \boldsymbol{F}_{Ad}$), the particles will be able to detach from the vessel wall under the action of the magnetic force. This force relationship has been termed as the sticking model in this work.

C. IMPLEMENTATION OF FLUID DYNAMICS

In order to maintain closeness to the real environments, it is important to define precise fluid dynamics inside the vessels. We have assumed that the blood flowing inside the vessel has a steady, laminar, creeping flow from the inlet to the outlet. In the simulation, the flow velocity profile throughout the vessel network is generated using the CFD module of COMSOL. However, since COMSOL cannot be used for real-time simulations, this velocity data is transferred to Unity 3D where the real-time simulation is processed. To verify the Unity 3D simulation results, we compared the trajectories for one particle generated by Unity 3D with those for the same particle generated by COMSOL for both the Y shaped and realistic blood vessel models (created and automatically meshed in SolidWorks). The trajectories are shown in Figure 5. For this test, the particle radius was 400nm and the average inlet velocity was selected as 10mm/s on the basis of a realistic blood velocity. It is clear from the images (Figure 5) that the trajectories generated by Unity 3D match those generated by COMSOL. Hence, the Unity 3D generated simulation results can be considered as a depiction of real particle behavior.

D. MAPPING METHOD BETWEEN HAPTICS AND MAGNETIC ACTUATORS SYSTEM

We have proposed the use of a haptic device to intuitively control the MNPs. However, since the position of MNPs is determined by various parameters inside the blood vessel, it is impossible to linearly map the linear movement of the haptic interaction point (HIP) onto the position of the MNPs. However, as shown in Table 2, we can map the haptic device position to the gradient of magnetic field using the value of current supplied to the actuation coils [39] (see Fig. 6).

The main goal of our tele-nano-robotic system is to guide the MNPs inside the virtual blood vessel by adjusting the appropriate magnitudes and directions of magnetic forces to change the positions of nanoparticles inside the vessel.

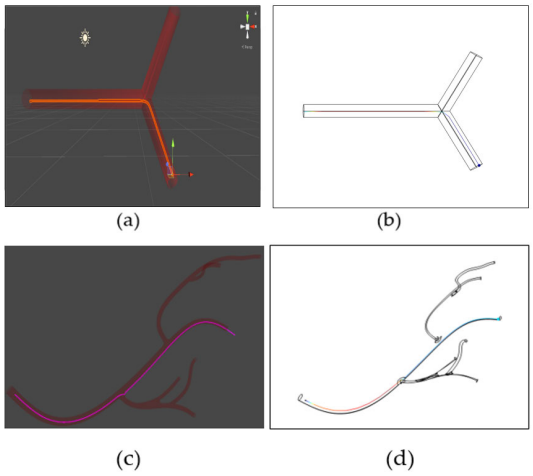

FIGURE 5. Particle trajectory with the same initial position of particle in Unity 3D ((a) and (c)) and in COMSOL ((b) and (d)). (a) and (b) are the particle trajectories in a Y-shaped channel. (c) and (d) are the particle trajectories in a realistic 3-D blood vessel model.

TABLE 2. Relationship between current and magnetic field gradient in single-coil-core system.

Current(A)	1	2	3	7	12	17
B(mT)	28.2	54.1	79.8	189	339	496.4
∇B(T/m)	0.43	0.92	1.39	3.27	5.57	8.06

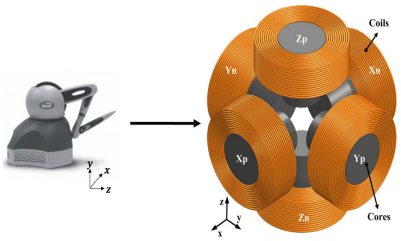

FIGURE 6. Mapping of the haptic device onto the 3D actuators.

In our system, we mapped the haptic device's deviation amounts along the x, y and z axes from a neutral home position to the input current of the electromagnetic actuators. The haptic device workspace is: -190 mm to $+190$ mm along x-axis, -130 mm to $+130$ mm along y-axis, and -90 mm to $+90$ mm along z-axis. Each workspace including its magnitude and direction information can be mapped to the current values from -17 A to 17 A for each actuator (x-direction: $\pm$ 0.089A/mm, y-direction: $\pm$0.13A/mm, z-direction: $\pm$0.19A/mm). In other words, we can linearly map the haptic position onto the magnetic force which can be applied to MNPs through electromagnetic actuators [33].

The magnetic force applied to MNPs becomes larger depending on the aggregation of MNPs. As shown in Figure 7, the magnetic force applied to a particle (generated with a constant current intensity) rapidly increases when the particles' radius is increased. Thus, the increase

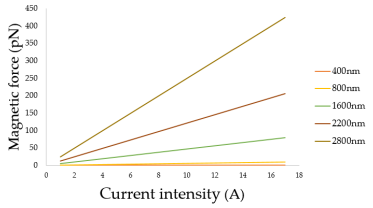

FIGURE 7. Magnetic force applied to particles of different sizes for different values of coil currents.

of particles' radius due to aggregation may result in bigger particles/aggregates, becoming easier to move at the same current intensity.

E. REALISTIC CHANNEL FOR SIMULATION

In the presented simulation we have utilized a brain vessel model that was reported in a previous work related to targeted drug delivery [22]. The geometric characteristics of the vessel model are shown in Figure 8. The model consists of one inlet for the inflow of blood flow and particles and six outlets. The paths have varied diameters, as shown in the figure.

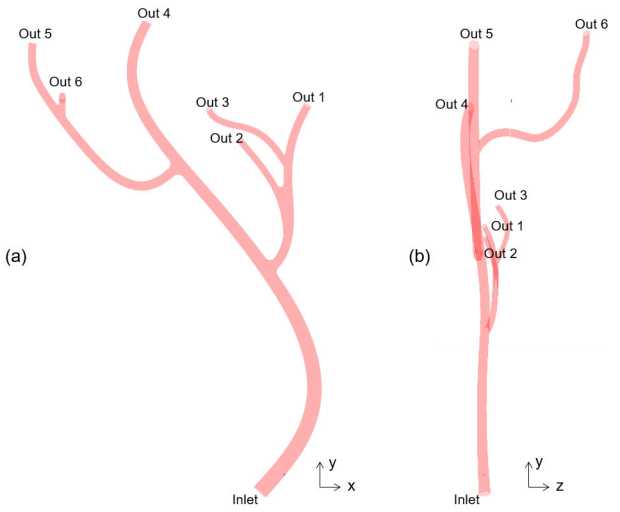

FIGURE 8. The realistic 3D model of a vessel inside the brain used in the simulation. Some of the geometric characteristics in terms of the size and shape of the vessels are presented. (a) The screen view provided to the user during the simulations (x-y plane). (b) y-z plane.

IV. ADAPTIVE FORBIDDEN REGION

As mentioned in the introduction section, we have suggested the use of adaptive forbidden region (AF) to cater to the aggregation phenomenon. We cannot set a standard point of control because the particles have a tendency of dispersing in the blood vessel. In this section, first we introduce the aggregation model that is used to determine the equivalent spherical radius of the particles after aggregation in order to increase the realism of the simulation. Second, we introduce the regional average concept used to generate a single point representing the particles inside the vessel, which is mapped to the haptic interaction point. Finally, we present the AF algorithm that adjusts the size of the forbidden region based on aggregation.

A. AGGREGATION MODEL

As mentioned above, when particles collide with each other, the equivalent spherical radius of the aggregated particle increases. However, there are no studies related to the degree of aggregation that occurs in targeted drug delivery. So, to include the aggregation effect in our simulation, we have defined an adhesion parameter (A_p). A_p is the ratio between the original equivalent radius of the particle before attachment and the new equivalent radius of the particle (aggregate) formed after the occurrence of attachment. It can be written as:

$$r_{eq} = r_{previous} A_p \tag{9}$$

where, r_{eq} is the equivalent radius after attachment and r_{previous} is the equivalent radius before attachment.

The A_p in our simulation was determined through the following experiment. 270 particles were released at the inlet of the brain vessel model and guided by the user to outlet 1, similar to the conditions [9] described in Table 1 (particle number is limited to 270 in order to maintain the 10Hz frame refresh rate under the processing constraints) (see Fig. 8). Outlet 1 was selected as the target in this simulation based on the previously reported works on particle navigation [19], [22]. However, further study may be required if a different target outlet is selected. The equivalent spherical radius of particles at the outlet was calculated (see Fig. 9). In this study, to match the simulation with previously reported experimental data [21], the maximum size of the aggregated magnetic particles' equivalent spherical radius is limited to 2.8 μm. It was found that an A_p value of just above 1.25 generates an equivalent spherical radius close to 2.8μm for almost all the particles, thus satisfying the size constraint [9]. Therefore, the adhesion parameter can be set between 1.0 and 1.25, to satisfactorily simulate the aggregation of particles inside the vessel.

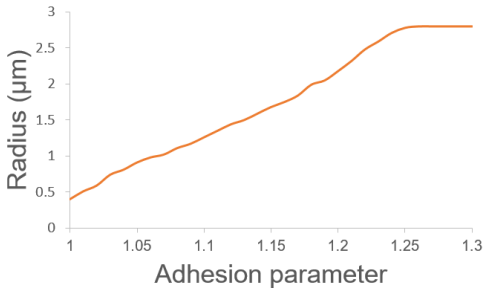

FIGURE 9. Particles radius according to adhesion parameter.

B. REGIONAL AVERAGE

In this simulation, since there is only one HIP that can control the displacements of nanoparticles, it is necessary to express these displacements as a single point in order to map them to the HIP. Thus, we suggest regional average concept.

Calculating regional average based on fixed regions [33] (red is region 1, yellow is region 2 and orange is region 3 in Figure 9(a)) is not suitable for more complex realistic vessel models (see Figure 10(b)).

FIGURE 10. (a)Calculating regional average position for HIP inside a Y-Shaped vessel with fixed regions. (b) A realistic 3D vessel model.

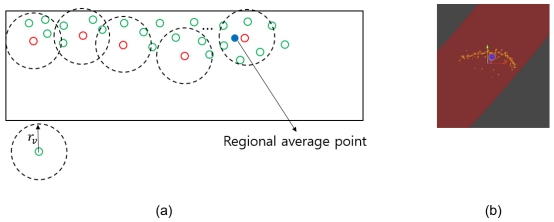

FIGURE 11. Regional average sphere for HIP with a virtual radius (r_v). (a) selection of the main regional average sphere with the highest number of particles (b) the demonstration of regional average sphere inside a 3D vessel (blue colored sphere).

In this paper, we suggest a novel method for calculating the regional average. In this algorithm, the point representing the position of each particle is made the center of a virtual sphere with a radius r_v (see Figure 11(a)). Then the number of particles lying inside this sphere is determined (N_n). Then, the regional average point is calculated from the particles lying inside the sphere with the highest value of N_n (see Figure 12). In case there exist two virtual spheres with the same highest number of MNPs (N_k and N_j), then the virtual sphere that is farthest from the inlet is used to calculate the regional average. This method has been adopted to ensure that the maximum number of particles can be guided to the intended branch of an oncoming bifurcation. If the regional average is formed close to the inlet, many particles may go to an unintended branch before the regional average point reaches the bifurcation. If the particles are close to the branch bifurcation and the value of r_v is high, the virtual sphere of a particle can include particles from the other branch. The regional average thus calculated can lie outside of either of the

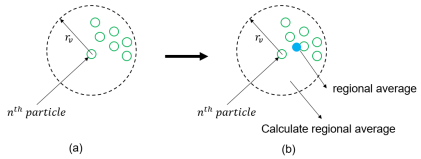

FIGURE 12. Steps for generating regional average. (a) the sphere centered on the nth particle is determined to have the highest number of particles N_n (b) calculation of the regional average which is the average position calculated from the positions of all the particles inside r_v centered on the n^{th} particle.

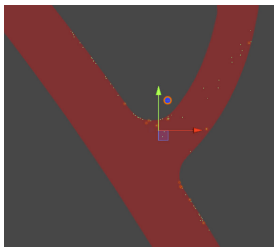

FIGURE 13. Regional average sphere outside the blood vessel with $r_v = 2$mm.

branches (see Figure 13). In order to avoid this, the value of r_v was fixed to 1 mm in this simulation. If the r_v is very small then the position of regional average can vary very abruptly. We observed the behavior of the average point for different values of r_v increasing in 0.1 mm steps from 0.5 mm to 3 mm and the value of 1mm was determined to have the best behavior. Following the abovementioned rules, the regional average point is generated as shown in Figure 11(b).

C. FORMATION OF ADAPTIVE FORBIDDEN REGION

In order to cater to the changes in particle behavior that occur due to aggregation, we propose the use of the adaptive forbidden region (AF) concept. Magnetic force acting on a particle is proportional to its radius. So, when aggregation occurs, the uneven action of forces on different particles causes an increase in the dispersion of particles. In order to deal with this phenomenon, AF based on the following equation is used.

$$r_{avg} = \frac{1}{N}\sum_{j=0}^{N} r_{eq}(j) \tag{10}$$

where, N is the number of particles inside the vessel, r_{eq}(j) is the equivalent spherical radius of particle and j is the index number of particles. This equation shows the average radius of the particles (r_{avg}). To know the relative radius ratio due to aggregation, we define the coefficient as follows;

$$C_A = \frac{r_{avg}}{r_i} \tag{11}$$

$$C_{max} = \frac{r_{max}}{r_i} \tag{12}$$

where r_i is the particle's initial radius, in this paper the initial radius is predetermined at 400nm, r_{max} is the maximum particle radius, d_v is the diameter of vessel, C_A is the aggregation coefficient and C_{max} is the maximum value of the aggregation coefficient. In order to cater to aggregation, height h_F of the forbidden region is adjusted as follows;

$$\begin{cases} C_A \le C_{max} * 0.9 \rightarrow h_F = \dfrac{d_v}{2} + \dfrac{1}{2}\dfrac{d_v}{(C_{max}-1)}(C_A - 1) \\ C_A > C_{max} * 0.9 \rightarrow h_F = \dfrac{d_v}{2} + \dfrac{1}{2}\dfrac{d_v}{(C_{max}-1)}(0.9C_{max} - 1) \end{cases} \tag{13}$$

when the value of the aggregation coefficient is close to the maximum aggregation coefficient value, the forbidden region is formed close to the vessel wall (i.e. $C_A = C_{max}$ and $h_F = d_v$). In this case, movement of the haptic device by

the user in any direction is restricted due to haptic feedback force (MNPs average point stays inside forbidden region). To prevent this situation, we set a saturation height limit ($0.94d_v$) on the forbidden region height (Figure 14(c)). The forbidden regions generated for different cases are shown in Figure 14.

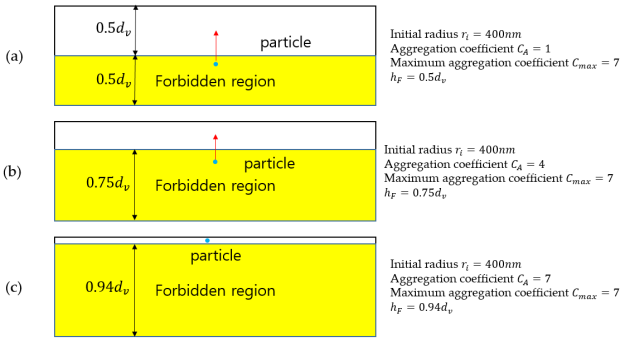

FIGURE 14. AF algorithm description. (a) no aggregation occurs and particle exists inside the forbidden region, (b) aggregation occurs and particle exists inside the forbidden region, and (c) maximum aggregation occurs.

V. SHARED CONTROL

When we simulate with the realistic 3D vessel model, we have to use 3-DOF actuators mapped to the 3D haptic device position (x-y-z). Consequently, the difference between the number of dimensions controlled by the user (3D) and those of the visualization (2D) can occur. As the screen can only provide a 2D visualization, the user must control the particles without any depth perception. This lack of perception can hinder the user's control ability, which can cause sticking of particles inside the vessel. In order to overcome this sticking phenomenon, particles' movement in the depth direction (along z axis in the current case) is controlled automatically while the movement in the two clearly visible dimensions is controlled by the user, thus forming a shared control paradigm. The basic concept of shared control is shown in Figure 15. Figures 15(a) and (b) show simple straight and branched vessel models, respectively. Figure 15(c) and Figure 15(d) show cross-sections of these models according to the guide plane. In the case of Figure 15(c), since there is no branch, it shows the cross-sectional view along the guide plane formed at the middle of the vessel. On the other hand, if a branch exists, the guide plane is set along the axis aligned with the direction of fluid flow, that passes through the center of the branch entrance in a direction that is normal to the entrance plane. For example, in Figure 15(b), since the fluid flows in the x-axis direction and the branch entrance is in the y-axis direction, the guide plane becomes the x-y plane passing through the center of the branch entrance (see Figure 15(d)). That is, z-axis is adjusted by automatic actuator control.

In summary, shared control is operated based on guide plane and regional average (see Fig. 16). The actuators automatically bring the particles to the guide plane and the feedback generated based on the regional average position helps the user guide the particles to the target. For example, when fluid flows in the y-direction after initial injection, particles are dispersed inside the vessel. The entrance of target branch exists in upper direction (x) of main vessel. Thus, guide plane is formed at xy-plane. To align the particles in xy-plane, a force along z-direction is applied by adjusting the duty cycle of the pulse functions that control the MNPs' average position in the xy-plane (see Figure 16(a)). To align the particles according to the guide plane of the vessel along the z-axis and to keep them in the xy-plane, the pulse function duty cycle (D_c) is applied. The D_c value of 0.4 generates a negative force along the z-axis to move the MNPs' average position downwards, while the D_c value of 0.6 moves it upwards towards the guide plane of the z-axis (see Figure 16(c)). D_c values were determined by trial and error to find the best performance in alignment. This was done by changing the value of D_c in steps of 0.1 and comparing the paritcle dispersions from the guide plane. The value resulting in the minimum dispersion was selected. Finally, particles are aligned along the guide plane determined using the aforementioned method and represented in Figure 16(d).

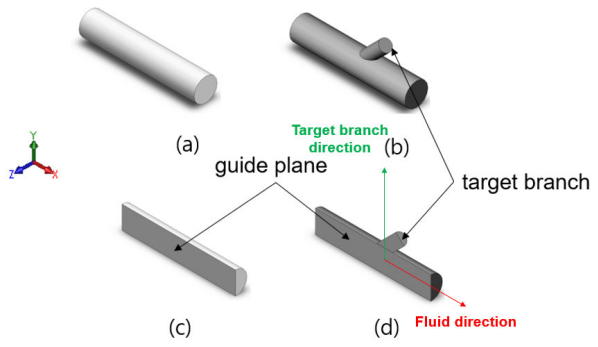

FIGURE 15. Principle of determining guide plane in simple straight (a), and branched (b) vessel models. (c) and (d) show the section views of the vessels according to the generated guide planes.

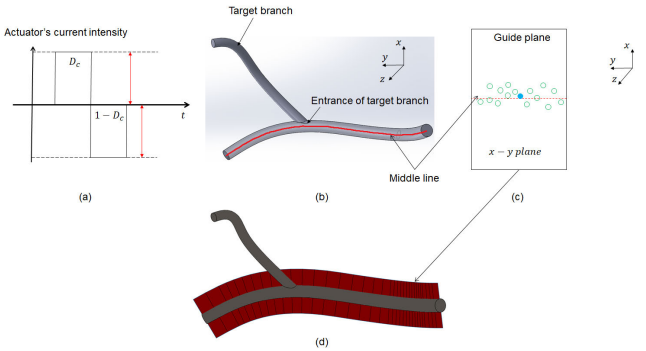

FIGURE 16. Alignment scheme applied using magnetic actuators. (a) pulse functions of the actuators, (b) 3D image of the vessel including the guide line (red), (c) particles aligned in the 2D plane (xy- plane) along the guide line (red) and (d) Conceptual representation of the guide plane (red) in a curved vessel.

VI. RESULT AND DISCUSSION

A. USER STUDIES

Six subjects (2 men and 4 women with an average age of 26 years) participated in the experiment. To demonstrate the efficiency of the integrated schemes in a 3D realistic vessel, five test modes were studied as follows; Default mode (D): particles move from an inlet to an outlet without any external forces. Visual feedback mode (V): the user should manipulate the particles while being provided with only the visual feedback from the Unity 3D screen, here the haptic device is used only as a joystick to steer the nanoparticles. Shared control mode (S): this mode changes the 3 DOF control to a 2 DOF control by constraining the particles into one plane; MNP movement along one axis is constrained automatically by magnetic actuators, while movement along two axes is actively controlled by the user through the haptic device which functions as a simple joystick in this mode. Visual feedback is provided through the screen. Shared control and forbidden region mode (S-F): combines the shared control scheme and forbidden region haptic feedback. Particle motion in one DOF is controlled by the automatic scheme. The user controls the particle position along the two remaining axes using the haptic device while receiving haptic and visual feedback. Shared control and adaptive forbidden region mode (S-AF): combines the shared control and adaptive forbidden region concept, which can restrict the MNPs' movements through haptic interaction by considering the aggregation effects of MNPs inside the vessel. At low fluid velocities, it is difficult to verify the effectiveness of the interaction mode because it is easier for the user to steer the MNPs. So, the fluid velocity in these experiments was set at 10 mm/s based on the blood velocity inside a real brain [9], [19]. 270 particles with the initial radius of 400nm, distributed uniformly at the inlet of the realistic 3D vessel model, were released into the channel (see Figure 8). Other simulation conditions for blood modeling are the same as presented in Table 1 and reported in [9]. Outlet 1 was selected as the target outlet. The simulation time is set as T_s =5 T_i [22], where T_i is the time taken by the particles to move from the inlet to the outlet without any external magnetic force, also referred as initial time. At the end of the simulation time, particles that are still inside the vessel are considered as the ''remaining particles''. Participants did not have any prior experience of working with a haptic device. So, each participant was allowed to try the system out a few times to become familiar with the virtual environment and the tele-nano-manipulation process. We analyzed two values: targeting ratio (the ratio of particles reaching the target outlet) and sticking ratio (the ratio of particles remaining inside the vessel at the end of the simulation) under different operation modes. Factors were defined as operation mode (4 levels: Visual mode (V); Shared-control mode (S); Shared-control and Forbidden region mode (S-F); Shared-control and Adaptive forbidden region mode (S-AF)) and fluid velocity (10 mm/s). We performed one-way Analysis of Variance (ANOVA). Significance level (α) was set at p-value < 0.05. All statistical analyses were performed using SPSS V20.0 (IBM Corp., Armonk, NY, USA).

B. RESULTS

Six participants took part in the study to evaluate the performance of different operation modes. The results of all participants are presented in Figure 17. There was significant interaction between the haptic mode and targeting ratio (see Figure 17(a)), and between the haptic mode and sticking ratio (Figure 17(b)). The overall data is presented in Table 3 as the averaged percentages of particles going to outlet 1 (target outlet) during the experiment (see Figure 8). From the ANOVA it was found that significant differences in the targeting ratio existed between V and S (p-value < 0.01), V and S-F (p-value < 0.01), V and S-AF (p-value < 0.01), S and S-AF (p-value < 0.01), and S-F and S-AF (p-value < 0.01). Whereas, there were no significant differences in the targeting ratio between S and S-F (p -value > 0.5) (see Fig. 17).

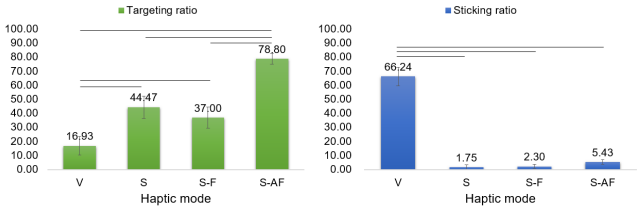

FIGURE 17. Effect of haptic modes on targeting rate (a) and sticking rate (b). Here each – represents a statistically significant difference between the two underlying conditions.

TABLE 3. Average ratio of particles in each outlet.

M	Reaching to outlets						Remain
	1	2	3	4	5	6	
D	**29.49**	8.40	4.12	32.13	4.04	0.0	21.82
V	**16.93**	0.67	0.00	12.75	0.00	0.00	66.24
S	**44.47**	2.43	1.06	50.71	0.00	0.00	1.75
S-F	**37.00**	0.67	1.43	55.70	0.00	0.00	2.30
S-AF	**78.80**	0.00	0.00	15.88	0.00	0.00	5.43

For the sticking ratio, it was found that significant differences existed between V and S (p-value < 0.01), V and S-F (p-value < 0.01), and V and S-AF (p-value < 0.01). However, there were no significant differences between S and S-AF (p-value > 0.5), S and S-F (p-value > 0.5), S and S-AF (p-value > 0.5), and S-F and S-AF (p-value > 0.5).

The particles remaining inside the vessel at the end of the simulation time (T_s) and the trajectories of particles under different operating modes with a representative subject are shown in Figures 18 and 19, respectively.

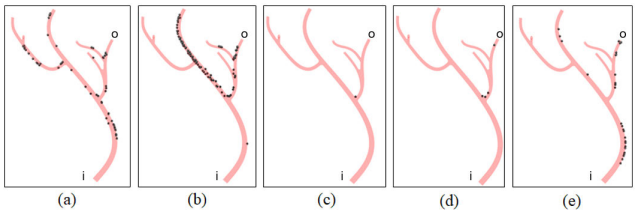

FIGURE 18. Particles remaining inside the vessel in each mode (i is inlet, o is outlet). (a) default (50/270), (b) visual feedback (181/270), (c) shared control (2/270), (d) shared control and forbidden region (4/270), and (e) shared control and adaptive forbidden region (15/270).

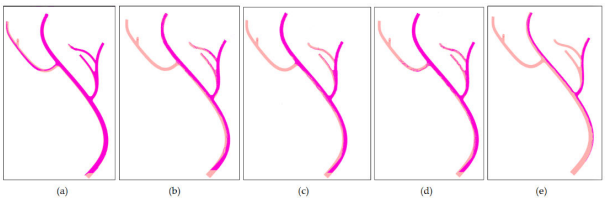

FIGURE 19. Trajectories for each mode (inlet and outlet is same with Figure 18). (a) default, (b) visual feedback, (c) shared control, (d) shared control and forbidden region, and (e) shared control and adaptive forbidden region.

1) EFFECTS OF USING SHARED CONTROL

In the Default mode, particles are spread over all the branches (see Fig. 18(a) and Fig. 19(a)). The particles are only moved by the flow velocity, so the trajectory of each particle depends on the vessel's geometric structure. In the visual feedback mode the user controls the magnetic field using the haptic device while viewing the visual feedback provided via the screen. In this mode, it can be seen that the number of particles exiting the outlet that is far away from the target outlet is reduced compared to the default mode (see Fig. 18(b)). However, the screen is limited to 2D and the user has to control the particles in 3D, so more particles are seen stuck inside the vessel than in the default mode (see Fig. 19(b)). In order to overcome this limitation, the proposed shared control method automatically aligns the particles to the guide plane, effectively reducing the user-controlled dimensions down to two. Thus, as shown in Figure 18(c), the use of shared control results in a reduction in the number of particles remaining inside the vessel.

2) EFFECTS OF USING THE ADAPTIVE FORBIDDEN REGION

The results of a representative subject using the shared control with the forbidden region and the adaptive forbidden region are shown in Figures 18 (d, e) and 19 (d, e). As mentioned in the previous section, using shared control can decrease the sticking of particles inside the vessel as compared to the D and V modes (see Fig 18(c), (d) and (e)). The forbidden region only provides a fixed limit of the movable area for the particles and is not affected by the amount of aggregation. Thus, it can be observed that addition of forbidden region to shared control does not greatly affect the particles' trajectory (see Fig. 19(c) and (d)). It can also be observed that the use of forbidden region with shared control only slightly increases the number of particles sticking inside the vessel (see Fig. 18(c) and Fig. 18(d)). In the case of the adaptive forbidden region, the height of the forbidden region is determined according to the average value of particles' equivalent radius. This results in application of greater movement limitations on larger particles that are more sensitive to control inputs, thus reducing the impact of user inexperience and/or mistakes on the targeting ratio. In the realistic scenario, a large amount of aggregation occurs so the adaptive forbidden region is formed close to vessel wall. Thus, as shown in Fig. 19(e), trajectories of the particles are formed closer to the vessel wall compared to those in Fig. 19(d). This forms a more compact swarm that can provide ease of particle guidance. However, it can be observed in Figure 18(e) that the number of particles sticking inside the vessel increases under the adaptive forbidden region condition. This may be due to the behavior of the adaptive forbidden region that pushes the particles close to the wall.

3) EFFECTS OF USING THE SHARED-CONTROL AND ADAPTIVE FORBIDDEN REGION

The targeting ratio and sticking ratio for each outlet are given in Table 3. Compared with the default mode (D), V mode can reduce the ratio particles going to undesired outlets (except for outlet 1). However, the sticking ratio is significantly increased due to the visual limitation. As a result, when we use a haptic interface independently without algorithms, we can reduce the ratio of particles going to undesired outlets but the haptic interface cannot overcome the sticking of MNPs inside the vessel due to the visual limitation. By applying the automatic alignment scheme (shared control), we can improve the targeting ratio and reduce the sticking ratio significantly. However, there are no significant differences in targeting ratio between the S mode and the S-F mode due to the dispersion of MNPs caused by aggregations. To overcome the dispersions, the S-AF mode can improve the targeting ratio significantly compared to the S mode and the S-F mode. Hence, we can improve the targeting ratio in the realistic vessel by using the AF algorithm, and we can reduce the sticking ratio by using the shared control scheme with automatic alignment of MNPs. However, using the AF may increase the sticking ratio as it causes the particles to move very close to the wall where some particles may enter the boundary layer of the fluid, thus removing them from the moving fluid stream.

Through these results, we can determine that the S-AF algorithm can improve targeting efficiency and reduce the sticking ratio inside the vessel.

C. DISCUSSSION

As highlighted in the introduction, previously developed targeted drug delivery systems that use open loop control have two main issues: lack of precise mathematical modeling, lack of navigation to a targeted position in complex realistic vessel. In this study, we presented a 3D navigation platform and proposed a novel algorithm (S-AF) to govern the use of

a haptic interface device for user in-the-loop navigation to solve the aforementioned issues. Specifically, we showed that by applying the adaptive forbidden region, we can cater to random aggregation. We also showed that by applying shared control, we can get rid of particles sticking inside the vessel.

Although S-AF algorithm is effective in targeted drug delivery, if there are a lot of branches and the distance between branch entrances is small, we can only achieve a targeting ratio of below 20 %. However, in cases where the branches are farther apart, we can achieve a targeting ratio of above 50%. One way of improving the targeting ratio is to increase the particles' size [40], which would increase the magnetic force acting on the particles. An alternative method can be to increase the magnetic field strength using cores inside the coils, which can generate high magnetic field strength with same amount of power supplied to the coils [41]. In order to reduce the dispersion of MNPs inside the vessels, the proposed system uses an algorithm based on the regional average of MNPs. Thus, if MNPs are dispersed inside the vessel, the precision of this algorithm is reduced. Consequently, the suggested algorithm is not effective for closely situated outlets such as outlets 2 and 3. The current work strived to elucidate the feasibility of swarm control for navigation of MNPs. Based on this work, the finer points of this method will be further refined in the future.

The algorithm requires several critical improvements to become suitable for *in-vivo* and *in-vitro* applications. These include acquisition of the actual geometric structure of real vessels using MRI and the use of MPI for particle imaging [42]. With the combination of these methodologies, we may be able to implement the developed algorithms to realize particle navigation inside real vessels.

VII. CONCLUSION

This paper presented a novel MNP swarm guidance algorithm for MTD in a realistic 3D vessel model using shared automatic control with adaptive haptic interaction. Through user studies in a realistic 3D environment generated using fluid dynamics modeled in COMSOL, it was observed that the proposed algorithm (S-AF) improved the performance of MTD. Results show that the S-AF can significantly improve the targeting ratio while reducing the sticking ratio when random aggregation occurs. The ultimate goal of our research is to realize remote control of MNPs in real blood vessels. So, in the future, we will integrate this system with an MPI system to perform *in-vitro* testing.

REFERENCES

[1] M. Sitti, H. Ceylan, W. Hu, J. Giltinan, M. Turan, S. Yim, and E. Diller, "Biomedical applications of untethered mobile milli/microrobots," *Proc. IEEE*, vol. 103, no. 2, pp. 205–224, Feb. 2015.

[2] B. J. Nelson, I. K. Kaliakatsos, and J. J. Abbott, "Microrobots for minimally invasive medicine," *Annu. Rev. Biomed. Eng.*, vol. 12, no. 1, pp. 55–85, Jul. 2010.

[3] M. P. Kummer, J. J. Abbott, B. E. Kratochvil, R. Borer, A. Sengul, and B. J. Nelson, "OctoMag: An electromagnetic system for 5-DOF wireless micromanipulation," *IEEE Trans. Robot.*, vol. 26, no. 6, pp. 1006–1017, Dec. 2010.

[4] J. Li, B. Esteban-Fernández de Ávila, W. Gao, L. Zhang, and J. Wang, "Micro/nanorobots for biomedicine: Delivery, surgery, sensing, and detoxification," *Sci. Robot.*, vol. 2, no. 4, Mar. 2017, Art. no. eaam6431.

[5] T. D. Do, F. U. Amin, Y. Noh, M. O. Kim, and J. Yoon, "Guidance of magnetic nanocontainers for treating Alzheimer's disease using an electromagnetic, targeted drug-delivery actuator," *J. Biomed. Nanotechnol.*, vol. 12, no. 3, pp. 569–574, Mar. 2016.

[6] Q. A. Pankhurst, J. Connolly, S. Jones, and J. Dobson, "Applications of magnetic nanoparticles in biomedicine," *J. Phys. D, Appl. Phys.*, vol. 36, no. 13, p. R167, 2003.

[7] S. D. Steichen, M. Caldorera-Moore, and N. A. Peppas, "A review of current nanoparticle and targeting moieties for the delivery of cancer therapeutics," *Eur. J. Pharmaceutical Sci.*, vol. 48, no. 3, pp. 416–427, Feb. 2013.

[8] B. Shapiro, S. Kulkarni, A. Nacev, S. Muro, P. Y. Stepanov, and I. N. Weinberg, "Open challenges in magnetic drug targeting," *Wiley Interdiscipl. Rev., Nanomedicine Nanobiotechnol.*, vol. 7, no. 3, pp. 446–457, May 2015.

[9] A. K. Hoshiar, T.-A. Le, and J. Yoon, "Electromagnetic actuation scheme for swarm of magnetic nanoparticles steering in multi-bifurcation," in *Proc. Int. Conf. Manipulation, Autom. Robot. Small Scales (MARSS)*, Jul. 2019, pp. 1–6.

[10] P. Vartholomeos, M. Fruchard, A. Ferreira, and C. Mavroidis, "MRI-guided nanorobotic systems for therapeutic and diagnostic applications," *Annu. Rev. Biomed. Eng.*, vol. 13, no. 1, pp. 157–184, Aug. 2011.

[11] A. Servant, F. Qiu, M. Mazza, K. Kostarelos, and B. J. Nelson, "Controlled *in vivo* swimming of a swarm of bacteria like microrobotic flagella," *Adv. Mater.*, vol. 27, no. 19, pp. 2981–2988, May 2015.

[12] E. U. Saritas, P. W. Goodwill, L. R. Croft, J. J. Konkle, K. Lu, B. Zheng, and S. M. Conolly, "Magnetic particle imaging (MPI) for NMR and MRI researchers," *J. Magn. Reson.*, vol. 229, pp. 116–126, Apr. 2013.

[13] N. B. Crane, O. Onen, J. Carballo, Q. Ni, and R. Guldiken, "Fluidic assembly at the microscale: Progress and prospects," *Microfluidics Nanofluidics*, vol. 14, nos. 3–4, pp. 383–419, Mar. 2013.

[14] A. S. Masoudi, M. S. Hassanli, Z. Taavili, and Y. Sadeghizade, "Biomedical and micro-robots: An overview of recent developments," *Chem. Biomol. Eng.*, vol. 2, no. 2, pp. 90–95, 2017.

[15] D. Laird, I. A. Raptis, and J. Price, "Design and validation of a centimeter-scale robot collective," in *Proc. IEEE Int. Conf. Syst., Man, Cybern. (SMC)*, Oct. 2014, pp. 918–923.

[16] F. Arvin, J. C. Murray, L. Shi, C. Zhang, and S. Yue, "Development of an autonomous micro robot for swarm robotics," in *Proc. IEEE Int. Conf. Mechatronics Autom.*, Aug. 2014, pp. 635–640.

[17] A. Shklarsh, A. Finkelshtein, G. Ariel, O. Kalisman, C. Ingham, and E. Ben-Jacob, "Collective navigation of cargo-carrying swarms," *Interface Focus*, vol. 2, no. 6, pp. 786–798, Dec. 2012.

[18] A.-R. Merheb, R. Mourad, A. Diab, and A. Haddad, "3D navigation algorithm of a micro-robot swarm in blood vessels for medical applications," in *Proc. 5th Int. Conf. Adv. Biomed. Eng. (ICABME)*, Oct. 2019, pp. 1–4.

[19] A. Hoshiar, T.-A. Le, F. Amin, M. Kim, and J. Yoon, "A novel magnetic actuation scheme to disaggregate nanoparticles and enhance passage across the blood–brain barrier," *Nanomaterials*, vol. 8, no. 1, p. 3, Dec. 2017.

[20] T.-A. Le, X. Zhang, A. K. Hoshiar, and J. Yoon, "An electromagnetic navigation system with real-time 2D magnetic particle imaging for targeted drug delivery," in *Proc. IEEE/RSJ Int. Conf. Intell. Robots Syst. (IROS)*, Sep. 2017, pp. 1895–1900.

[21] A. K. Hoshiar, T.-A. Le, F. U. Amin, M. O. Kim, and J. Yoon, "Studies of aggregated nanoparticles steering during magnetic-guided drug delivery in the blood vessels," *J. Magn. Magn. Mater.*, vol. 427, pp. 181–187, Apr. 2017.

[22] M. D. Tehrani, J.-H. Yoon, M. O. Kim, and J. Yoon, "A novel scheme for nanoparticle steering in blood vessels using a functionalized magnetic field," *IEEE Trans. Biomed. Eng.*, vol. 62, no. 1, pp. 303–313, Jan. 2015.

[23] J. Yu, L. Yang, and L. Zhang, "Pattern generation and motion control of a vortex-like paramagnetic nanoparticle swarm," *Int. J. Robot. Res.*, vol. 37, no. 8, pp. 912–930, Jul. 2018.

[24] S. Chowdhury, W. Jing, and D. J. Cappelleri, "Controlling multiple microrobots: Recent progress and future challenges," *J. Micro-Bio Robot.*, vol. 10, nos. 1–4, pp. 1–11, Oct. 2015.

[25] A. R. Lanfranco, A. E. Castellanos, J. P. Desai, and W. C. Meyers, "Robotic surgery: A current perspective," *Ann. surgery*, vol. 239, no. 1, p. 14, 2004.

[26] L. Thurfjell, J. McLaughlin, J. Mattsson, and P. Lammertse, "Haptic interaction with virtual objects: The technology and some applications," *Ind. Robot, Int. J.*, vol. 29, no. 3, pp. 210–215, Jun. 2002.
[27] Christiand and J. Yoon, "Assembly simulations in virtual environments with optimized haptic path and sequence," *Robot. Comput.-Integr. Manuf.*, vol. 27, no. 2, pp. 306–317, Apr. 2011.
[28] J. Yoon and P. Kumar, "A novel optimal assembly algorithm for haptic interface applications of a virtual maintenance system," *J. Mech. Sci. Technol.*, vol. 23, no. 1, pp. 183–194, Jan. 2009.
[29] S. H. Syed Hassan and J. Yoon, "Haptic based optimized path planning approach to virtual maintenance assembly/disassembly (MAD)," in *Proc. IEEE/RSJ Int. Conf. Intell. Robots Syst.*, Oct. 2010, pp. 1310–1315.
[30] A. M. Okamura, "Haptic feedback in robot-assisted minimally invasive surgery," *Current Opinion Urol.*, vol. 19, no. 1, p. 102, 2009.
[31] L. B. Rosenberg, "Virtual fixtures: Perceptual tools for telerobotic manipulation," in *Proc. IEEE Virtual Reality Annu. Int. Symp.*, Oct. 1993, pp. 76–82.
[32] M. Hong and J. W. Rozenblit, "A haptic guidance system for computer-assisted surgical training using virtual fixtures," in *Proc. IEEE Int. Conf. Syst., Man, Cybern. (SMC)*, Oct. 2016, pp. 2230–2235.
[33] V. Hamdipoor, M. Afzal, T.-A. Le, and J. Yoon, "Haptic-based manipulation scheme of magnetic nanoparticles in a multi-branch blood vessel for targeted drug delivery," *Micromachines*, vol. 9, no. 1, p. 14, Jan. 2018.
[34] R. Taylor, P. Jensen, L. Whitcomb, A. Barnes, R. Kumar, D. Stoianovici, P. Gupta, Z. Wang, E. Dejuan, and L. Kavoussi, "A steady-hand robotic system for microsurgical augmentation," *Int. J. Robot. Res.*, vol. 18, no. 12, pp. 1201–1210, Dec. 1999.
[35] R. A. MacLachlan, B. C. Becker, J. C. Tabares, G. W. Podnar, L. A. Lobes, and C. N. Riviere, "Micron: An actively stabilized handheld tool for microsurgery," *IEEE Trans. Robot.*, vol. 28, no. 1, pp. 195–212, Feb. 2012.
[36] S. L. Charreyron, B. Zeydan, and B. J. Nelson, "Shared control of a magnetic microcatheter for vitreoretinal targeted drug delivery," in *Proc. IEEE Int. Conf. Robot. Autom. (ICRA)*, May 2017, pp. 4843–4848.
[37] B. Issa, I. Obaidat, B. Albiss, and Y. Haik, "Magnetic nanoparticles: Surface effects and properties related to biomedicine applications," *Int. J. Mol. Sci.*, vol. 14, no. 11, pp. 21266–21305, Oct. 2013.
[38] J. Rahmer, D. Wirtz, C. Bontus, J. Borgert, and B. Gleich, "Interactive magnetic catheter steering with 3-D real-time feedback using multi-color magnetic particle imaging," *IEEE Trans. Med. Imag.*, vol. 36, no. 7, pp. 1449–1456, Jul. 2017.
[39] A. Mahmood, M. Dadkhah, M. Ok Kim, and J. Yoon, "A novel design of an MPI-based guidance system for simultaneous actuation and monitoring of magnetic nanoparticles," *IEEE Trans. Magn.*, vol. 51, no. 2, pp. 1–5, Feb. 2015.
[40] Z. W. Tay, D. W. Hensley, E. C. Vreeland, B. Zheng, and S. M. Conolly, "The relaxation wall: Experimental limits to improving MPI spatial resolution by increasing nanoparticle core size," *Biomed. Phys. Eng. Express*, vol. 3, no. 3, May 2017, Art. no. 035003.
[41] X. Zhang, T.-A. Le, A. K. Hoshiar, and J. Yoon, "A soft magnetic core can enhance navigation performance of magnetic nanoparticles in targeted drug delivery," *IEEE/ASME Trans. Mechatronics*, vol. 23, no. 4, pp. 1573–1584, Aug. 2018.
[42] J. Salamon, M. Hofmann, C. Jung, M. G. Kaul, F. Werner, K. Them, R. Reimer, P. Nielsen, A. vom Scheidt, G. Adam, T. Knopp, and H. Ittrich, "Magnetic particle/magnetic resonance imaging: *In-vitro* MPI-guided real time catheter tracking and 4D angioplasty using a road map and blood pool tracer approach," *PLoS ONE*, vol. 11, no. 6, Jun. 2016, Art. no. e0156899.

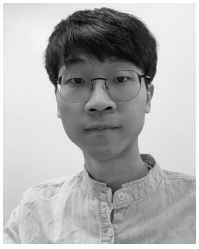

MYUNGJIN PARK received the B.E. degree in electrical and electronic engineering from Handong University, Pohang, South Korea, in 2019. He is currently pursuing the Integrated Ph.D. degree in mechanical engineering with the School of Integrated Technology, Gwangju Institute of Science and Technology, Gwangju, South Korea. His current research interests include bio-nano robot control and electromagnetic navigation systems.

TUAN-ANH LE received the M.Sc. degree in electrical engineering from the Hanoi University of Science and Technology, Hanoi, Vietnam, in 2013. He is currently pursuing the Ph.D. degree with the Gwangju Institute of Science and Technology, Gwangju, South Korea. From 2014 to 2017, he was a Researcher and a Ph.D. candidate with Gyeongsang National University, Jinju, South Korea. In 2018, he joined the School of Integrated Technology, Gwangju Institute of Science and Technology. His current research interests include electromagnetics, actuators, magnetic particle imaging, bio-nano robot control, hyperthermia, and brain stimulation.

AMRE EIZAD was born in Peshawar, Pakistan, in 1987. He received the B.E. degree in mechatronics engineering and the M.S. degree in mechatronics engineering from Air University, Islamabad, Pakistan, in 2009 and 2011, respectively. He is currently pursuing the Ph.D. degree in mechanical engineering with Gyeongsang National University, Jinju, South Korea.

He was a Lab Engineer (from 2009 to 2011) and a Lecturer (from 2011 to 2016) with the Department of Mechatronics Engineering, Air University. His research interest includes the development of robotic rehabilitation systems for people with motor disorders.

JUNGWON YOON (Member, IEEE) received the Ph.D. degree from the Department of Mechatronics, Gwangju Institute of Science and Technology (GIST), Gwangju, South Korea, in 2005.

From 2005 to 2017, he was a Professor with the School of Mechanical and Aerospace Engineering, Gyeongsang National University, Jinju, South Korea. In 2017, he joined the School of Integrated Technology, GIST, where he is currently an Associate Professor. He has authored or coauthored more than 80 peer-reviewed journal articles and patents. His current research interests include bio-nano robot control, virtual reality haptic devices, and rehabilitation robots. He is a Technical Editor of the IEEE/ASME TRANSACTIONS ON MECHATRONICS and an Associate Editor of *Frontiers in Robotics and AI*.